J. Fluid Mech. (1995), *vol.* 299, *pp.* 105–132

Lateral capillary interaction between particles protruding from a spherical liquid layer

By P. A. KRALCHEVSKY[1], V. N. PAUNOV[1] AND KUNIAKI NAGAYAMA[2]

[1] Laboratory of Thermodynamics and Physico-chemical Hydrodynamics, University of Sofia, Faculty of Chemistry, Sofia 1126, Bulgaria

[2] Protein Array Project, ERATO, JRDC; 5-9-1 Tokodai, Tsukuba 300-26, Japan

(Received 26 September 1994 and in revised form 16 February 1995)

The lateral capillary interaction between two particles immersed in a spherical thin liquid film is investigated. The interfacial shape, the lateral capillary force and the interparticle interaction energy are calculated by using the numerical solution of the linearized Laplace equation of capillarity. Orthogonal bipolar coordinates on a sphere (inducing biconical coordinates in space) are introduced as a helpful instrument for solving this problem and other problems of similar geometry. We consider two types of boundary conditions at the particle surfaces: fixed contact *angle* and fixed contact *line*. We established that for particles of fixed contact angle the capillary interaction energy depends monotonically on the interparticle distance whereas for particles of fixed contact line the interaction energy exhibits a maximum. The numerical results show that in both cases the capillary interaction is much larger than the thermal energy kT and can induce aggregation and ordering of submicrometre particles. These theoretical findings can be important for understanding the properties of Pickering emulsions (stabilized by particles) and liposomes or biomembranes containing incorporated membrane proteins.

1. Introduction

The lateral capillary interaction between particles attached to a liquid–fluid interface is due to the overlap of the menisci formed around each of the particles. In the case of floating particles of diameters greater than about 10 μm the interaction occurs because the gravitational potential energy of the particles decreases when they approach each other (Nicolson 1949; Chan, Henry & White 1981; Paunov *et al.* 1993). This force is proportional to R^6 (R is the particle radius), so it decreases fast with particle size and becomes negligible for $R < 10$ μm. It was recently established that the situation is quite different when the particles, instead of being freely floating, are partially immersed in a liquid layer (Kralchevsky *et al.* 1992, 1993; Kralchevsky & Nagayama 1994). In this case the energy of lateral capillary attraction is proportional to R^2 and turns out to be much larger than the thermal energy kT even with particles of diameter about 10 nm. This effect is related to the particle three-phase contact angle, i.e. to the intermolecular forces, rather than to gravity. The physical importance of these 'immersion'-type lateral capillary forces is that they bring about the formation of two-dimensional arrays (2D-crystals) from both micrometre-size colloidal particles (Denkov *et al.* 1992, 1993) and submicrometre particles, including protein globules (Yoshimura *et al.* 1990; Nagayama 1994). It is worthwhile noting that these forces can be directly measured (Camoin *et al.* 1987; Velev *et al.* 1993).

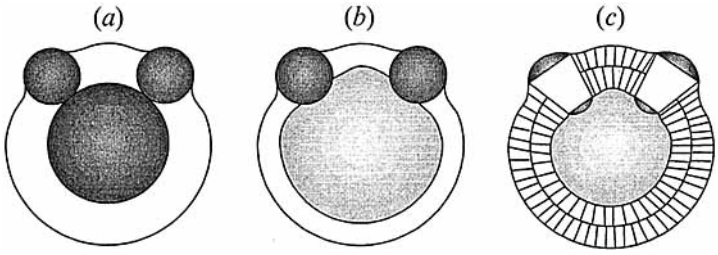

FIGURE 1. Sketch of three possible configurations of particles protruding from a spherical liquid film: (*a*) two particles immersed in a thin liquid film on a solid spherical substrate; (*b*) two particles included in a vesicle; (*c*) two membrane proteins incorporated into a lipid bilayer.

The available theoretical studies of lateral immersion forces are restricted to particles confined in *planar* liquid layers. The present article is devoted to the calculation of such forces for the case of *spherical* liquid layers. The spherical geometry implies some specific conditions not present in planar films. For example, the volume of the liquid layer is finite. In addition, the capillary force between two diametrically opposed particles is always zero irrespective of the range of the capillary interaction determined by the capillary length, q^{-1}, see equation (2.10) below.

Examples of systems containing spherial layers are shown in figure 1. A solid particle (substrate) covered with a liquid film between the substrate and the outer fluid phase is sketched in figure 1 (*a*); such configurations can appear in some suspensions. Smaller particles incorporated in the liquid layer interact through the perturbations in the shape of the liquid-fluid interface caused by them.

Figure 1 (*b*) shows a similar system, but with two liquid interfaces: the spherical film is between an emulsion droplet and the outer fluid phase. In this case the particles immersed in the film deform both fluid interfaces.

A spherical lipid bilayer (vesicle) containing incorporated membrane proteins is depicted in figure 1 (*c*). The difference in the thickness of the hydrophobic zones of the protein and the bilayer gives rise to interfacial deformations and protein–protein interaction (Israelachvili 1977). The peculiarity of this system is that the hydrocarbon core of the lipid bilayer exhibits some elastic behaviour and cannot be treated as a simple fluid (Petrov & Bivas 1984).

In summary, we deal with relatively small particles contained in a liquid phase; hence, we can assume that the effect of gravity on the interfacial shape is negligible. At these conditions the (non-disturbed) spherical liquid film may have stable uniform thickness only due to the action of some repulsive surface forces inside the film (Derjaguin, Churaev & Muller 1987; Israelachvili 1992). For this reason we will consider only thin liquid films below, i.e. films in which the effect of the surface forces (the disjoining pressure) is not negligible.

As mentioned above, the aim of the present study is to calculate the lateral capillary force between two particles which are partially immersed in a spherical film. To solve this problem we first need to find the shapes of the fluid interfaces, which depend on the boundary conditions at the particle three-phase contact lines. We will consider two types of boundary conditions at the particle surface: (i) fixed contact angle, and (ii) fixed contact line. Case (i) corresponds to equilibrium wetting; for example, if the particle is well wettable by the liquid of the film, the contact angle will be zero irrespective of the position of the contact line. Case (ii) occurs when the contact line is attached to some edge or to the boundary between hydrophobic and hydrophilic zones on the particle surface, see e.g. figure 1 (*c*).

A variety of systems and configurations is possible; in the present study we restrict our considerations to the simpler case depicted in figure 1(*a*), where there is only one deformable interface and the two particles are identical. We believe the methodology developed in the present article can be further extended to more complicated systems, like those depicted in figure 1(*b*) (*two* deformable interfaces) or 1(*c*) (film with *elastic* behaviour).

The paper is structured as follows. In §2 we formulate the mathematical problem and calculate the interfacial shape by numerical integration of Laplace equation of capillarity. In §3 we determine the force and energy of capillary interaction as functions of interparticle separation by integrating the stresses exerted on the particle surfaces. The numerical results are presented and discussed in §4.

Note that here we solve the hydrostatic problem, i.e. we suppose that the two interacting particles are kept fixed at a given distance apart by some external force. Of course, if the external force is removed, the two particles will move towards each other under the combined action of capillary attraction and viscous friction. The solution of the hydrostatic problem considered below is a prerequisite for the solution of the more sophisticated dynamic problem.

To calculate the meniscus shape and the lateral capillary forces in the case of a planar film it is convenient to use bipolar coordinates in the plane (Kralchevsky *et al.* 1992). Analogously, in the case of a spherical film it is convenient to utilize orthogonal bipolar coordinates on a sphere, which induce biconical coordinates in space (see the Appendix). We believe this system of curvilinear coordinates introduced by us is of independent interest as it can be applied to the solution of various problems of hydrodynamics, the theory of elasticity and capillarity. In the Appendix we derive the respective expressions for the metric tensor, Christoffel symbols, rate-of-strain tensor and Navier–Stokes equation in terms of these coordinates.

The method for calculating the lateral capillary forces developed below as well as the curvilinear coordinates introduced may be applied to any physical problem dealing with particles attached to a spherical fluid interface or thin liquid film. Such problems can appear in the theory of Pickering emulsions, which are stabilized by the adsorption of small particles onto the surface of emulsion droplets (Levine & Bowen 1991), cf. figure 1(*b*). Another field of application is the hydrodynamics of 'froth flotation', studying hydrophobic particle attachment to rising air bubbles (Dukhin, Ruliov & Dimitrov 1986). Similarly, the spherical bipolar coordinates can be useful for the calculation of the hydrodynamic interaction between membrane proteins incorporated in spherical lipid bilayers (vesicles, figure 1*c*) or biomembranes (cf. Bussel, Koch & Hammer 1992).

2. Calculation of the interfacial shape

2.1. *Description of the system*

Let us consider a spherical solid substrate of radius R_s covered with a liquid film (F) between the substrate (I) and the outer fluid phase (II), figure 2. The wetting film (F) is spherical in the absence of incorporated particles because of the existence of repulsion (disjoining pressure) between the two film surfaces (Derjaguin *et al.* 1987; Israelachvili 1992).

The presence of particles which are partially immersed in the film (figure 2) leads to a deviation of the outer film surface from sphericity. Below we restrict our considerations to film thicknesses and particle sizes much smaller than R_s. An *auxiliary* system is depicted in figure 2(*a*), in which the two particles have a very special shape:

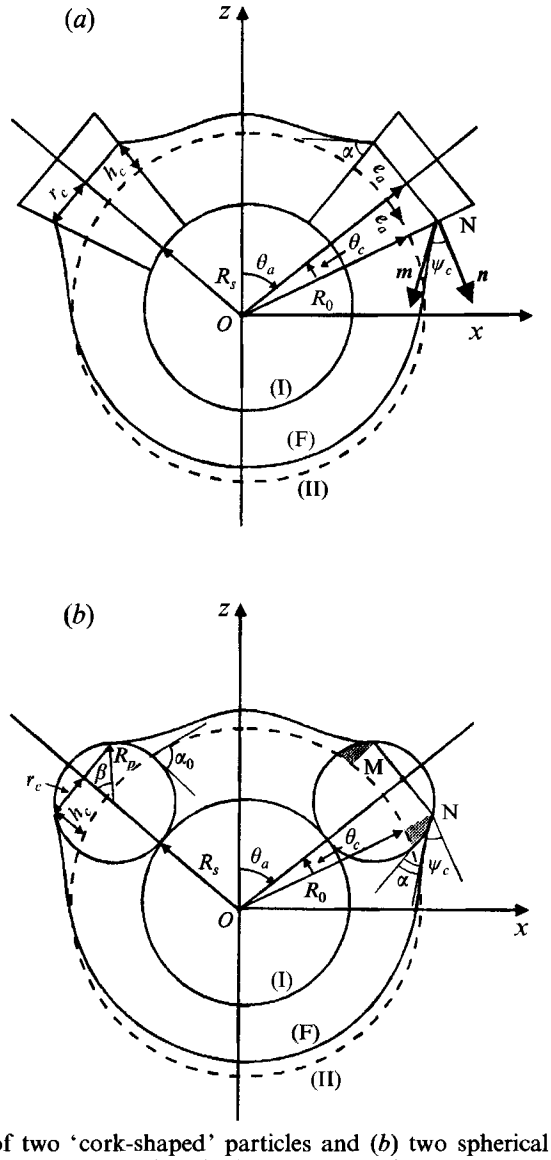

FIGURE 2. (*a*) Sketch of two 'cork-shaped' particles and (*b*) two spherical particles of radius R_p protruding from a liquid layer on a solid spherical substrate of radius R_s. r_c is the radius of the three-phase contact line, the angles θ_a and θ_c characterize the particle positions and sizes, h_c is the elevation of the contact line above the level of the reference sphere of radius R_0. Note that in both (*a*) and (*b*) ψ_c is defined as the angle between the normal to the segment ON and the tangent to the meniscus.

part of a slender cone with vertex in the substrate centre. For brevity such particles are called below 'cork-shaped particles'. It will be demonstrated below that the consideration of this system is useful for the subsequent treatment of the more realistic system with two spherical particles depicted in figure 2(*b*). Correspondingly, the further considerations based on 'cork-shaped' particles are extended to spherical particles in §4 below. In addition, it should be mentioned that the shape of some membrane proteins can be represented approximately by truncated cones (Israelachvili 1992).

The deviation of the outer film surface from sphericity is caused by the capillary rise

of the liquid along the particle surface in order for an equilibrium contact angle, α, to be formed. For given values of the radii of the substrate and particles, and for a fixed volume of the film, there is one special value, α_0, of the contact angle (figure 2*b*), which corresponds to a spherical interface between the film and phase II ($\alpha_0 = \pi/2$ for the configuration in figure 2*a*). We denote the radius of this sphere by R_0 and will call it the *reference sphere*. It is shown dashed in figure 2. For $\alpha < \alpha_0$ the film will be deformed as shown in figure 2. In this case the radial (normal) resultant of the capillary forces will press the particles against the substrate. (If $\alpha > \alpha_0$ the capillary forces will tend to detach the particle from the substrate; this case is not considered in the present study.)

The radial coordinate, r, of a point on the deformed film surface can be represented in the form

$$r = R_0 + \zeta(\theta, \phi) \tag{2.1}$$

where θ and ϕ are the polar and azimuthal angles in spherical coordinates. We assume small deformation:

$$|\zeta/R_0| \ll 1 \quad \text{and} \quad |\nabla_{II}\zeta|^2 \ll 1, \tag{2.2}$$

where ∇_{II} denotes surface gradient operator on the reference sphere. At static conditions ζ obeys the Laplace equation of capillarity (see Landau & Lifshitz 1984; Kralchevsky & Ivanov 1990), which can be linearized in view of (2.2):

$$P_R + \Pi(h) - P_{II} = \gamma(h)\left[\frac{2}{R_0} - \frac{2\zeta}{R_0^2} - \nabla_{II}^2\zeta\right]. \tag{2.3}$$

Here P_{II} is the pressure in the outer fluid (*II*), P_R is the reference pressure in the thin liquid film (for a definition of P_R see (2.18) below), Π is the disjoining pressure, and γ is the interfacial tension of the boundary film/phase II. Both Π and γ depend on the film thickness

$$h = h_0 + \zeta, \quad h_0 = R_0 - R_s = \text{const.} \tag{2.4}$$

2.2. *Disjoining pressure and film surface tension*

In view of (2.2) one can use the relation between γ and Π for a plane-parallel film (Ivanov & Toshev 1975)

$$\gamma(h) = \gamma_\infty + \int_h^\infty \Pi(h)\,\mathrm{d}h, \tag{2.5}$$

where γ_∞ is the surface tension of the bulk liquid phase (infinitely thick film) and the integral term expresses the work (per unit area) performed by the surface forces to bring the two film surfaces from infinity to a finite distance h. Then if $\zeta \ll h_0$ one can use the expansions

$$\Pi = \Pi_0 + \Pi'\zeta + \ldots, \tag{2.6}$$

$$\gamma = \gamma_0 - \Pi_0\zeta - \tfrac{1}{2}\Pi'\zeta^2 + \ldots, \tag{2.7}$$

where

$$\gamma_0 = \gamma|_{h=h_0}, \quad \Pi_0 = \Pi|_{h=h_0}, \quad \Pi' = \left.\frac{\mathrm{d}\Pi}{\mathrm{d}h}\right|_{h=h_0}. \tag{2.8}$$

By substituting (2.6) and (2.7) in (2.3) and keeping the linear terms one obtains

$$\nabla_{II}^2\zeta - q^2\zeta = 2\Delta H, \quad \zeta \ll R_0, \tag{2.9}$$

where

$$q^2 = -\frac{\Pi'}{\gamma_0} - \frac{2}{R_0^2} - \frac{2\Pi_0}{\gamma_0 R_0} \tag{2.10}$$

and

$$\Delta H = \frac{1}{R_0} - \frac{1}{R}, \quad \frac{1}{R} \equiv \frac{1}{2\gamma_0}(P_R + \Pi_0 - P_{II}). \tag{2.11}$$

The derivative of disjoining pressure is negative, $\Pi' < 0$, for a stable film (Derjaguin *et al.* 1987). Moreover, we assume that $|\Pi'|$ is large enough to have $q^2 > 0$; q^{-1} has the meaning of capillary length, which determines the range of the lateral capillary forces. For $R_0 \to \infty$ (2.10) reduces to the respective expression for a planar thin liquid film in the absence of gravity (cf. Kralchevsky *et al.* 1992).

ΔH in (2.11) represents the change in the mean curvature of the film surface due to the deformation created by the two particles immersed in the film. R can be interpreted as the outer radius of an imaginary spherical layer of thickness h_0, whose internal pressure is equal to the pressure inside the perturbed film.

2.3. *Interfacial deformation and 'capillary charge'*

To estimate ΔH we will make use of the fact that the volume of the liquid film does not change in the investigated range of capillary pressures, i.e. liquid can be regarded as incompressible. The volume

$$V_m = \int_{S_0}\int \mathrm{d}\theta\,\mathrm{d}\phi \int_{R_0}^{R_0+\zeta} \mathrm{d}r\, r^2 = \int_{S_0} \mathrm{d}s\left(\zeta + \frac{\zeta^2}{R_0} + \frac{\zeta^3}{3R_0^2}\right) \tag{2.12}$$

is to be equal to zero (the integration is over the region S_0 representing the radial projection of the deformed interface on the reference sphere). $V_m = 0$ is a rigorous equation for the configuration in figure 2(*a*) and an approximated expression for the configuration in figure 2(*b*); in the latter case the approximation consists in neglecting some volumes shown shaded in figure 2(*b*), which are small enough when $R_p \ll R_0$. By means of (2.2), (2.9) and (2.12) one obtains

$$0 = V_m \approx \int_{S_0} \mathrm{d}s\,\zeta = q^{-2}\int_{S_0} \mathrm{d}s(\nabla_{II}^2\zeta - 2\Delta H). \tag{2.13}$$

Using the Green–Gauss–Ostrogradsky theorem (Weatherburn 1939; Brand 1947; McConnell 1957) one obtains

$$\int_{S_0} \mathrm{d}s\,\boldsymbol{\nabla}_{II}\cdot(\boldsymbol{\nabla}_{II}\zeta) = \sum_{k=1}^{2}\oint_{C_k} \mathrm{d}l\boldsymbol{\nu}\cdot\boldsymbol{\nabla}_{II}\zeta, \tag{2.14}$$

where C_k ($k = 1, 2$) are orthogonal projections of the two contact lines onto the reference sphere of radius R_0; $\mathrm{d}l$ is linear element, $\boldsymbol{\nu}$ is a unit normal to C_k which is simultaneously tangential to the reference sphere; note that $\boldsymbol{\nu}$ is directed toward the interior of the region encircled by C_k, $k = 1, 2$. Then

$$\oint_{C_k} \mathrm{d}l\boldsymbol{\nu}\cdot\boldsymbol{\nabla}_{II}\zeta = 2\pi r_0 \tan\psi_c, \quad r_0 = R_0\sin\theta_c, \tag{2.15}$$

where $\tan\psi_c$ is the average meniscus slope at the contact line and r_0 is the radius of the radial projection of the contact line on the reference sphere. (For the configuration in figure 2(*a*) $\psi_c = \pi/2 - \alpha = \text{const.}$ and one can directly write $\boldsymbol{\nu}\cdot\boldsymbol{\nabla}_{II}\zeta = \tan\psi_c$.)

From (2.2) and (2.13)–(2.15) we derive

$$\Delta H \approx \frac{Q}{2R_0^2}, \quad \frac{r_0^2}{R_0^2} \ll 1, \tag{2.16}$$

where

$$Q \equiv r_0\sin\psi_c \approx r_0\tan\psi_c \tag{2.17}$$

is called the 'capillary charge' (Paunov *et al.* 1993) since it characterizes the interfacial deformation created by each of the particles and the resulting capillary interaction

between them. (In particular, for planar geometry the lateral capillary force between two particles of capillary charges Q_1 and Q_2 obeys asymptotically a two-dimensional analogue of Coulomb's law: $F = -2\pi\gamma Q_1 Q_2/L$ with L being the interparticle distance; the term 'capillary charge' originates from this analogy with electrostatics.) A comparison between (2.16) and (2.11) yields an expression determining the reference pressure inside the film:

$$P_R = P_{II} - \Pi_0 + \frac{2\gamma_0}{R_0} - \frac{\gamma_0 Q}{R_0^2}. \tag{2.18}$$

Equations (2.17) and (2.18) show that both Q and P_R depend on the boundary condition at the particle three-phase contact lines.

2.4. *Curvilinear coordinates and boundary conditions*

By introducing the variable

$$\tilde{\zeta} = (\zeta + 2q^{-2}\Delta H)/R_0 \tag{2.19}$$

(2.9) obtains in the form

$$\nabla_{II}^2 \tilde{\zeta} = q^2 \tilde{\zeta}. \tag{2.20}$$

The geometry of the system implies the introduction of bipolar coordinates (τ, σ) on the reference sphere. These orthogonal curvilinear coordinates are described in detail in the Appendix. The geometrical parameters R_0, θ_c and θ_a (figure 2) are assumed known. By means of (A 7) in the Appendix and some geometrical considerations one determines the parameter λ of the bipolar coordinates:

$$\lambda = \frac{\cos\theta_c}{\cos\theta_a} \quad (\theta_a \geqslant \theta_c). \tag{2.21}$$

Note that $1 < \lambda < \infty$; in particular $\lambda = 1$ when the two particles in figure 2(*a*) touch each other, while $\lambda = \infty$ when the particles are diametrically opposed.

The contours C_1 and C_2 (representing the lines of intersection of the cork-shaped particles with the reference sphere) correspond to $\tau = \pm\tau_c = \text{const.}$; the corresponding value of parameter ξ (see the Appendix) we denote by ξ_c. Some geometrical considerations yield $\xi_c = \cot\theta_a$; then by using (2.21) and (A 14) one determines

$$\tau_c = \operatorname{arctanh}[(\lambda^2-1)^{1/2}\cot\theta_a] = \operatorname{arctanh}\left(\frac{(\cos^2\theta_c - \cos^2\theta_a)^{1/2}}{\sin\theta_a}\right). \tag{2.22}$$

In terms of the spherical bipolar coordinates (2.20) takes the form

$$(\lambda\cosh\tau - \cos\sigma)^2\left(\frac{\partial^2\tilde{\zeta}}{\partial\sigma^2} + \frac{\partial^2\tilde{\zeta}}{\partial\tau^2}\right) = (qR_0)^2(\lambda^2-1)\tilde{\zeta}(\sigma,\tau), \tag{2.23}$$

cf. (A 29) and (A 31) in the Appendix. Let us first consider the configuration depicted in figure 2(*a*). In the case of *fixed contact angle* the boundary conditions at the contours C_1 and C_2 read

$$\boldsymbol{\nu}\cdot\nabla_{II}\zeta = (-1)^k \tan\psi_c \quad \text{at contour } C_k \quad (k = 1, 2), \tag{2.24}$$

where $\boldsymbol{\nu}$ has the same meaning as in (2.15). By using (A 28) and (A 29) one transforms the boundary condition (2.24) to read

$$\left.\frac{\partial\tilde{\zeta}}{\partial\tau}\right|_{\tau=\tau_c} = \frac{\sin\psi_c(\lambda^2-1)^{1/2}}{(\lambda\cosh\tau_c - \cos\sigma)} \quad \text{(fixed contact angle)}, \tag{2.25}$$

$k = 1, 2$. As mentioned earlier, an alternative boundary condition of *fixed contact line*, $\zeta = h_c = \text{const.}$, can be used. In this case by means of (2.15)–(2.17), (2.19) and (A 23) we obtain

$$\tilde{\zeta}|_{\tau=\tau_c} = \frac{h_c}{R_0} + \frac{1}{\pi q^2 R_0^2}\int_0^\pi d\sigma \left.\frac{\partial\tilde{\zeta}}{\partial\tau}\right|_{\tau=\tau_c} \quad \text{(fixed contact line)}, \tag{2.26}$$

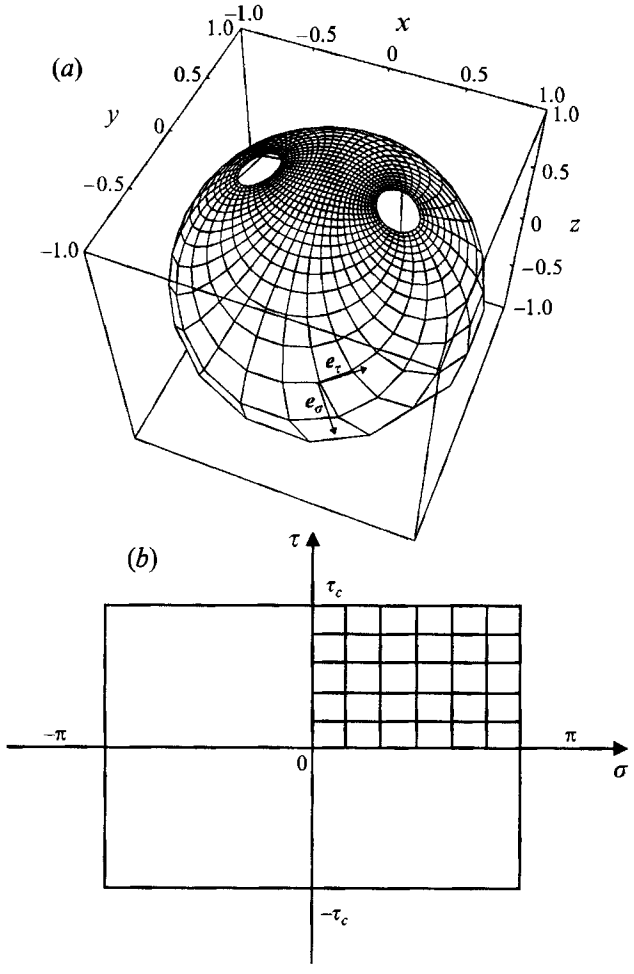

FIGURE 3. (*a*) Bipolar coordinate lines on the unit sphere. The lines $\tau = \text{const.}$ ($\xi = \text{const.}$) are counterparts of the parallels, whereas the lines $\sigma = \text{const.}$ ($\eta = \text{const.}$) connect the two poles and in this respect resemble meridians. (*b*) The integration domain on the reference sphere reduces to a rectangle in bipolar coordinates on a sphere.

$k = 1, 2$. The latter boundary condition is applicable for both configurations depicted in figure 2.

2.5. *Calculation procedure and results*

The input dimensionless parameters characterizing the liquid film are h_0/R_0 and qR_0. The input parameters characterizing the particles are θ_a, θ_c and h_c/R_0 (or α) when the contact line (or the contact angle) on the particle is fixed. Then one calculates λ and τ_c by means of (2.21) and (2.22). The distance between the two particles is characterized by the length of the (shortest) arc in the reference sphere connecting the axes of the two particles: $L = 2\theta_a R_0$. In the numerical calculations we use the dimensionless length

$$\tilde{L} = L/(\pi R_0) = 2\theta_a/\pi; \quad 2\theta_c/\pi \leqslant \tilde{L} \leqslant 1. \tag{2.27}$$

As we use bipolar coordinates on the reference sphere the domain of integration of (2.23) represents a rectangle in the (σ, τ)-plane (see figure 3*a*, *b*), which is bounded by the lines $\sigma = \pm\pi$ and $\tau = \pm\tau_c$. Because of the symmetry we consider only a quarter of

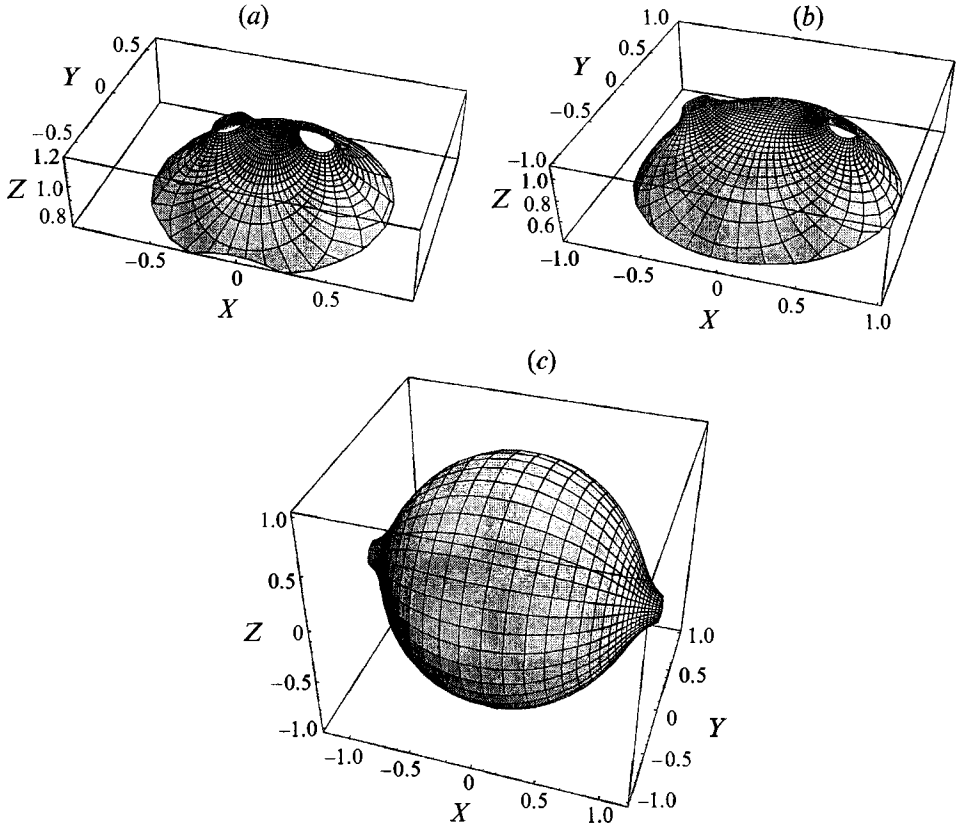

FIGURE 4. Plot of the calculated meniscus surface around two particles of fixed contact angle, $\psi_c = 20°$, $\theta_c = 5°$ and $qR_0 = 3$. The dimensionless coordinates are $X = x/R_0$, $Y = y/R_0$, $Z = z/R_0$. (*a*) Particles at a relatively small separation: $\theta_a = 15°$; (*b*) particles at an intermediate distance: $\theta_a = 35°$, and (*c*) two diametrically opposed particles, $\theta_a = 90°$.

this area corresponding to $0 \leqslant \sigma \leqslant \pi$ and $0 \leqslant \tau \leqslant \tau_c$; the respective boundary conditions implied by the symmetry are

$$\left.\frac{\partial\tilde{\zeta}}{\partial\sigma}\right|_{\sigma=0} = \left.\frac{\partial\tilde{\zeta}}{\partial\sigma}\right|_{\sigma=\pi} = 0 \tag{2.28}$$

and

$$\left.\frac{\partial\tilde{\zeta}}{\partial\tau}\right|_{\tau=0} = 0. \tag{2.29}$$

The latter condition holds only when the two particles are similar. The rectangular shape of the integration domain considerably simplifies and accelerates the numerical solution of the problem. We used the classical finite difference scheme of second order for discretization of the boundary problem. In this way for each node of the integration network we obtained one linear algebraic equation. The resulting set of equations was solved by means of the Gauss–Seidel iterative method (Korn & Korn 1968; Constantinides 1987) combined with successive over-relaxation (SOR) and the Chebyshev acceleration technique (Hockney & Easwood 1981).

First we will consider the case of fixed contact angle. For this case the calculated meniscus shape $\zeta(\sigma,\tau)$ around the two cork-shaped particles is depicted in figure 4(*a–c*). Figure 4(*a*) shows a case of close approach $\theta_a = 15°$, figure 4(*b*) illustrates the

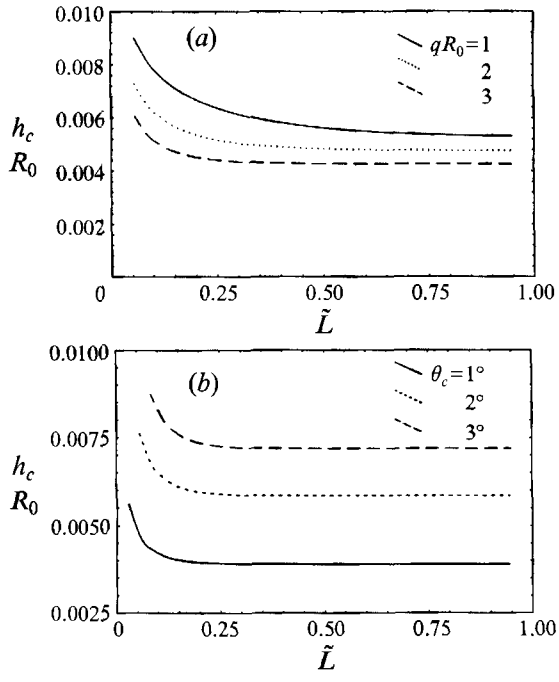

FIGURE 5. The dimensionless average capillary elevation, h_c/R_0, as a function of the dimensionless interparticle distance, $\tilde{L}$. (*a*) qR_0 is varied at $\theta_c = 2°$ and $\psi_c = 3°$; (*b*) θ_c is varied at $qR_0 = 5$ and $\psi_c = 5°$.

case of an intermediate separation, $\theta_a = 35°$, whereas figure 4(*c*) presents the limiting case of diametrically opposed particles, $\theta_a = 90°$. For $\theta_a = 15°$ and $\theta_a = 35°$ the meniscus intersects the reference sphere in the 'southern' hemisphere (not shown in figure 4*a*, *b*), where $\zeta(\sigma,\tau)$ changes from positive to negative. The reason is the condition for constant volume of the liquid layer, cf. (2.13).

In figures 5(*a*) and 5(*b*) the average capillary elevation

$$\tilde{h}_c \equiv \frac{h_c}{R_0} \equiv \frac{1}{2\pi r_0 R_0}\oint_{C_k} \zeta_c \,\mathrm{d}l$$

$$= \frac{(\lambda^2-1)^{1/2}}{\pi \sin\theta_c}\int_0^{\pi} \frac{\tilde{\zeta}(\sigma,\tau_c)\,\mathrm{d}\sigma}{\lambda\cosh\tau_c - \cos\sigma} - \frac{\sin\psi_c \sin\theta_c}{q^2 R_0^2} \tag{2.30}$$

of the liquid at the contact line C_k (figure 2) is plotted against the dimensionless interparticle separation, $\tilde{L}$.

The three curves in figure 5(*a*) correspond to different values of qR_0. The values of the other parameters (being the same for the three curves) are $\theta_c = 2°$ and $\psi_c = 3°$. One sees that $h_c \neq 0$ even for diametrically opposed particles, $\tilde{L} = 1$; this is due to the fact that the contact line is elevated even for a single particle because of the capillary rise. When the distance between the two particles decreases, the elevation h_c increases because of the overlap of the two menisci. As q^{-1} characterizes the dimension of such a meniscus, at fixed $\tilde{L}$ the overlap is greater (and, consequently, h_c is larger) when q^{-1} is greater, i.e. qR_0 is smaller, see figure 5(*a*).

Figure 5(*b*) represents h_c/R_0 *vs.* $\tilde{L}$ for three different values of θ_c and a fixed value of the particle slope angle, $\psi_c = 5°$. The radius R_0 is also fixed, but the radius of the

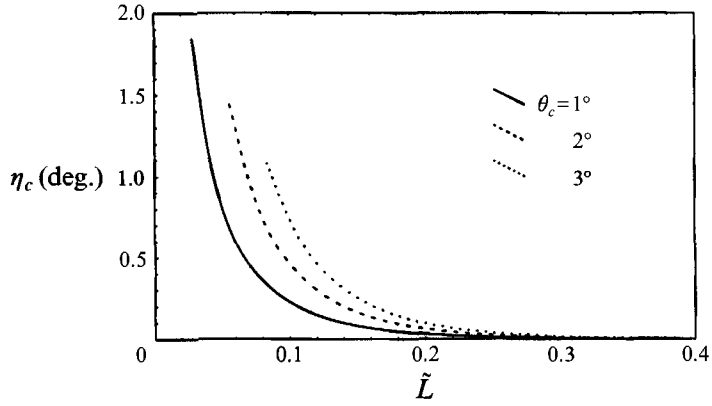

FIGURE 6. Plot of the contact line inclination angle, η_c, against the dimensionless interparticle distance, $\tilde{L}$, for three different values of the angle θ_c. The other parameters are the same as in figure 5(*b*).

contact line, $r_0 = R_0 \sin\theta_c$, increases with the increase of θ_c. In contrast with the parameter qR_0 (see figure 5*a*), the influence of the angle θ_c (i.e. of r_0/R_0) on the capillary elevation, h_c, is seen mainly in different values of the level, h_∞, of the contact line at $\tilde{L} = 1$. The behaviour of h_∞ is qualitatively similar to that of the elevation on a thin needle (fibre), see e.g. Kralchevsky *et al.* (1992); in the latter case $h_\infty \propto r_0 \sin\psi_c$, i.e. the elevation is greater for a needle of greater radius, r_0, and higher wettability (greater ψ_c). In principle, the volume of liquid displaced by a particle also increases with the increase of r_0, but this effect is of a higher order ($\propto r_0^2/R_0^2$) and does not affect significantly the value of h_∞, as far as small particles are concerned, cf. (2.16).

When the contact angle at the particle surfaces is fixed but the contact line is mobile the shape of the latter

$$\zeta_c(\sigma) \equiv \zeta(\tau_c, \sigma) \tag{2.31}$$

depends on σ, i.e. the contact line is not parallel to the reference sphere. The inclination of the contact line can be characterized by the angle η_c, defined as follows:

$$\tan\eta_c \equiv \frac{\zeta_c(\pi) - \zeta_c(0)}{2r_c} = \frac{\tilde{\zeta}_c(\pi) - \tilde{\zeta}_c(0)}{2(1+\tilde{h}_c)\sin\theta_c}, \tag{2.32}$$

where $r_c = (R_0 + h_c)\sin\theta_c$. Note that the angle, η_c, is zero in the cases of a single particle or two diametrically opposed particles. However, in the general case of two particles for $\tilde{L} < 1$ the angle η_c is not zero (see figure 7 below). The dependence of the inclination angle on the interparticle distance, $\tilde{L}$, is illustrated in figure 6 for three different values of the angle, θ_c (i.e. r_0/R_0) and fixed value of the particle contact angle ($\psi_c = 5°$). Note that η_c is a relatively small quantity even for short separations $\tilde{L}$. In spite of that, this small inclination is the reason for the appearance of strong lateral capillary interaction between the particles in the spherical liquid layer – see below.

When the boundary condition at the particle surface corresponds to fixed contact line, (2.26), the problem can be simplified considerably if one seeks a solution in the form

$$\tilde{\zeta}(\sigma, \tau) = Af(\sigma, \tau), \quad A = \text{const.}, \tag{2.33}$$

where the constant A is determined as explained below. The function $f(\sigma, \tau)$ obviously

satisfies equation (2.20) and the boundary conditions (2.28) and (2.29) with f instead of $\tilde{\zeta}$. Then we impose the requirement

$$\tilde{\zeta}|_{\tau=\tau_c} = A \quad \text{or} \quad f|_{\tau=\tau_c} = 1 \tag{2.34}$$

and from the boundary condition (2.26) we derive

$$A = \frac{h_c}{R_0} \Big/ \left(1 - \frac{1}{\pi q^2 R_0^2} \int_0^\pi \mathrm{d}\sigma \left.\frac{\partial f}{\partial \tau}\right|_{\tau=\tau_c}\right). \tag{2.35}$$

Thus, we first solve the boundary problem for $f(\sigma, \tau)$, then we calculate A from (2.35) and finally we get $\tilde{\zeta}(\sigma, \tau)$ from (2.33).

3. Lateral capillary forces

3.1. *Contributions due to surface tension and capillary pressure*

Let us consider one of the two particles, say the right-hand particle depicted in figure 2. The capillary force exerted on the particle can be obtained by integrating the interfacial tension along the contact line, C, and the pressure throughout the particle surface, S (Kralchevsky *et al.* 1993):

$$\boldsymbol{F} = \boldsymbol{F}^{(\gamma)} + \boldsymbol{F}^{(p)}, \tag{3.1}$$

$$\boldsymbol{F}^{(\gamma)} = \oint_C \mathrm{d}l\, \boldsymbol{m}\gamma, \quad \boldsymbol{F}^{(p)} = \oint_S \mathrm{d}s(-\boldsymbol{n})p, \tag{3.2}$$

where p is pressure, $\boldsymbol{n}$ is the outer unit normal to the particle surface and $\boldsymbol{m}$ is the unit vector in the direction of the surface tension γ; $\boldsymbol{m}$ is simultaneously perpendicular to the contact line and tangential to the liquid interface.

As in our case (figure 2) the particles are pressed against a solid substrate by the capillary forces, the resultant of $\boldsymbol{F}$ along the normal to the substrate is counterbalanced by the bearing reaction. Our aim below is to calculate the tangential component of $\boldsymbol{F}$.

Let $\boldsymbol{e}_a$ be the unit vector of the particle axis (figure 2*a*). We denote by $\boldsymbol{e}_t$ a unit vector in the plane (x, z), which is normal to $\boldsymbol{e}_a$ and tangential to the reference sphere. Then in view of the symmetry of the system our task is reduced to the calculation of the projections

$$F_t = \boldsymbol{e}_t \cdot \boldsymbol{F}, \quad F_t^{(\gamma)} = \boldsymbol{e}_t \cdot \boldsymbol{F}^{(\gamma)}, \quad F_t^{(p)} = \boldsymbol{e}_t \cdot \boldsymbol{F}^{(p)}. \tag{3.3}$$

Below we calculate F_t for the cases of fixed contact line and contact angle separately.

3.2. *Boundary condition of fixed contact line*

In this case

$$\zeta = h_c = \text{const.} \quad \text{(at the contact line)}. \tag{3.4}$$

Then the symmetry of the system implies $F_t^{(p)} = 0$. However, $F_t^{(\gamma)}$ is not zero because the meniscus slope

$$\tan\psi = \left.\frac{1}{\chi}\frac{\partial \zeta}{\partial \tau}\right|_{\tau=\tau_c} \tag{3.5}$$

(χ is defined in (A 29)) varies along the contact line. Let us denote by $\boldsymbol{e}_r$, $\boldsymbol{e}_\tau$ and $\boldsymbol{e}_\sigma$ the unit vectors of the local basis induced by the biconical coordinates (r, τ, σ), see figure 3(*a*) and the Appendix. For the points on the contact line one can write (figure 2*a*)

$$\boldsymbol{m} = -\boldsymbol{e}_\tau \cos\psi - \boldsymbol{e}_r \sin\psi. \tag{3.6}$$

As the contact line is a circumference, it is convenient to introduce polar coordinates (ρ, ϕ) in a plane perpendicular to the particle axis. Let $\boldsymbol{e}_\rho$ and $\boldsymbol{e}_\phi$ be the respective unit vectors. Then for the points on the contact line one has

$$\boldsymbol{e}_\tau = -\boldsymbol{e}_\rho \cos\theta_c + \boldsymbol{e}_a \sin\theta_c, \quad \boldsymbol{e}_t = \boldsymbol{e}_\rho \sin\theta_c + \boldsymbol{e}_a \cos\theta_c. \tag{3.7}$$

In addition, $\boldsymbol{e}_t \cdot \boldsymbol{e}_\rho = \cos\phi$ and $\boldsymbol{e}_t \cdot \boldsymbol{e}_a = 0$. From (3.6) and (3.7) one derives

$$\boldsymbol{e}_t \cdot \boldsymbol{m} = (\cos\theta_c \cos\psi - \sin\theta_c \sin\psi)\cos\phi. \tag{3.8}$$

Since we work with small deformations, see (2.2), we can write approximately

$$\cos\psi \approx 1 - \frac{1}{2}\left(\frac{1}{\chi}\frac{\partial\zeta}{\partial\tau}\right)^2_{\tau=\tau_c}, \quad \sin\psi \approx \left(\frac{1}{\chi}\frac{\partial\zeta}{\partial\tau}\right)_{\tau=\tau_c}, \tag{3.9}$$

cf. (3.5). From (3.2), (3.3), (3.8) and (3.9) one obtains

$$F_t = -\gamma_0 r_c \int_0^\pi \mathrm{d}\phi \cos\phi \left[\frac{1}{\chi^2}\left(\frac{\partial\zeta}{\partial\tau}\right)^2 \cos\theta_c + \frac{2}{\chi}\frac{\partial\zeta}{\partial\tau}\sin\theta_c\right]_{\tau=\tau_c}, \tag{3.10}$$

where $r_c = (R_0 + h_c)\sin\theta_c$ is the radius of the contact line and terms of higher order are neglected.

By solving (2.23) we determine ζ as a function of the bipolar coordinates (τ, σ). Therefore it is convenient to use σ for parametrization of the contact line, instead of the azimuthal angle ϕ. Some geometrical considerations yield

$$\tan\phi = \frac{y}{x'}; \quad x' = x\cos\theta_a - z\sin\theta_a. \tag{3.11}$$

Then from (2.22), (3.11) and (A 21) we derive

$$\cos\phi = \frac{\lambda\cosh\tau_c\cos\sigma - 1}{\lambda\cosh\tau_c - \cos\sigma}, \tag{3.12}$$

$$\frac{\mathrm{d}\phi}{\mathrm{d}\sigma} = \frac{(\lambda^2\cosh^2\tau_c - 1)^{1/2}}{\lambda\cosh\tau_c - \cos\sigma}. \tag{3.13}$$

Finally, by using (2.19), (3.1), (3.3), (3.10), (3.12), (3.13), (A 19) and (A 29) one can derive

$$\tilde{F}_t \equiv \frac{F_t}{\gamma_0 R_0} \approx -\int_0^\pi \mathrm{d}\sigma(\lambda\cosh\tau_c\cos\sigma - 1)\left[\frac{1}{(\lambda^2-1)^{1/2}}\left(\frac{\partial\tilde{\zeta}}{\partial\tau}\right)^2 + \frac{2\sin\theta_c}{\lambda\cosh\tau_c - \cos\sigma}\frac{\partial\tilde{\zeta}}{\partial\tau}\right]_{\tau=\tau_c}. \tag{3.14}$$

3.3. *Boundary condition of fixed contact angle*

The main difference with the previous subsection is that the contact line does not lie in a plane perpendicular to the particle axis. (In general, the inclination of the contact line increases when the interparticle distance decreases, see figure 6 above as well as the work by Velev *et al.* 1993.) Consequently, $F_t^{(p)}$ is no longer zero and the interfacial tension varies along the contact line in accordance with (2.7). (Note that in the case of fixed contact line, ζ and γ are constant along the contact line.) From (2.7), (3.2) and (3.3) one obtains

$$F_t^{(\gamma)} = \oint_C \mathrm{d}l(\boldsymbol{e}_t \cdot \boldsymbol{m})(\gamma_0 - \Pi_0\zeta_c + \ldots), \tag{3.15}$$

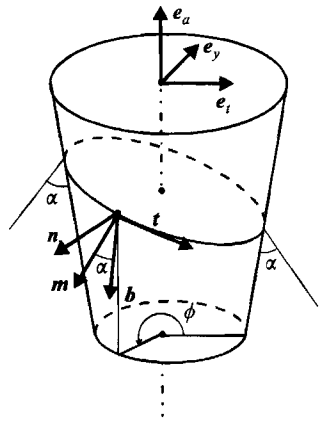

FIGURE 7. Sketch of the three-phase contact line of the right-hand-side cork-shaped particle (figure 2*a*). α is contact angle, $\boldsymbol{n}$ and $\boldsymbol{b}$ are the normal and binormal to the contact line, $\boldsymbol{m}$ is the running unit tangent to the meniscus surface and $\boldsymbol{t}$ is the tangent to the contact line.

where ζ_c is defined by (2.31). Let $\boldsymbol{t}$ be the running unit tangent to the contact line and, as usual, $\boldsymbol{n}$ be the outer unit normal to the particle surface (figure 7). Then

$$\boldsymbol{m} = \boldsymbol{b}\sin\psi_c + \boldsymbol{n}\cos\psi_c, \quad \boldsymbol{b} \equiv \boldsymbol{t}\times\boldsymbol{n}, \tag{3.16}$$

where $\psi_c = \pi/2 - \alpha$ and $\boldsymbol{b}$ it the unit binormal (figure 7). The unit vectors $\boldsymbol{e}_t$, $\boldsymbol{e}_y$ and $\boldsymbol{e}_a$ form an orthogonal basis. One can derive

$$\boldsymbol{n} = \boldsymbol{e}_t\cos\theta_c\cos\phi + \boldsymbol{e}_y\cos\theta_c\sin\phi - \boldsymbol{e}_a\sin\theta_c. \tag{3.17}$$

Also

$$\boldsymbol{t} = \frac{1}{t_c}\frac{\partial \boldsymbol{R}}{\partial\phi}, \quad \boldsymbol{R} \equiv (R_0+\zeta_c)\boldsymbol{e}_r, \tag{3.18}$$

where

$$t_c^2 = (R_0+\zeta_c)^2\sin^2\theta_c + \left(\frac{\mathrm{d}\zeta_c}{\mathrm{d}\phi}\right)^2, \quad \boldsymbol{e}_r = \boldsymbol{e}_t\sin\theta_c\cos\phi + \boldsymbol{e}_y\sin\theta_c\sin\phi + \boldsymbol{e}_a\cos\theta_c. \tag{3.19}$$

By using (3.17)–(3.19) one obtains

$$\boldsymbol{e}_t\cdot\boldsymbol{m} = -\frac{1}{t_c}\left[\frac{\mathrm{d}\zeta_c}{\mathrm{d}\phi}\cos^2\theta_c\sin\phi + \frac{\mathrm{d}(|\boldsymbol{R}|\sin\phi)}{\mathrm{d}\phi}\sin^2\theta_c\right]\sin\psi_c + \cos\theta_c\cos\psi_c\cos\phi.$$

Then (3.15) can be transformed to read

$$F_t^{(\gamma)} = -2\gamma_0\cos\theta_c(\cos\theta_c\sin\psi_c + \sin\theta_c)\int_0^\pi \mathrm{d}\phi\frac{\mathrm{d}\zeta_c}{\mathrm{d}\phi}\sin\phi$$
$$+\frac{\gamma_0}{r_0}\cos\theta_c\int_0^\pi \mathrm{d}\phi\left(\frac{\mathrm{d}\zeta_c}{\mathrm{d}\phi}\right)^2\cos\phi - 2\Pi_0 r_0\cos\theta_c\int_0^\pi \mathrm{d}\phi\,\zeta_c\cos\phi, \tag{3.20}$$

where higher-order terms have been neglected.

Next we consider $F_t^{(p)}$. On substituting (Kralchevsky & Nagayama 1994)

$$p = \begin{cases} P_R & \text{for} \quad R_0 \leqslant r \leqslant \zeta_c \\ P_{II} & \text{for} \quad r \geqslant \zeta_c, \end{cases} \tag{3.21}$$

in (3.2), by means of (3.3), (3.18) and (3.21) we obtain

$$F_t^{(p)} = -\cos\theta_c \sin\theta_c \int_0^{2\pi} \mathrm{d}\phi \cos\phi \left(P_R \int_{r_1}^{R_0+\zeta_c} r\,\mathrm{d}r + P_{II} \int_{R_0+\zeta_c}^{r_2} r\,\mathrm{d}r \right), \tag{3.22}$$

where r_1 and r_2 satisfy the relationship $r_1 \leqslant \zeta_c(\phi) \leqslant r_2$ for any ϕ; the exact choice of r_1 and r_2 is not important because $F_t^{(p)}$ does not depend on them. Indeed, after some transformations and neglecting higher-order terms, (2.18) and (3.22) lead to

$$F_t^{(p)} = 2(\Pi_0 - 2\gamma_0/R_0)\, r_0 \cos\theta_c \int_0^{\pi} \mathrm{d}\phi\, \zeta_c \cos\phi. \tag{3.23}$$

The combination of (3.20) and (3.23), in keeping with (3.1) and (3.3), finally yields

$$F_t = -2\gamma_0 \cos\theta_c (\cos\theta_c \sin\psi_c - \sin\theta_c) \int_0^{\pi} \frac{\mathrm{d}\zeta_c}{\mathrm{d}\phi} \sin\phi\,\mathrm{d}\phi + \frac{\gamma_0}{r_0} \cos\theta_c \int_0^{\pi} \mathrm{d}\phi \left(\frac{\mathrm{d}\zeta_c}{\mathrm{d}\phi}\right)^2 \cos\phi \tag{3.24}$$

(in (3.23) we have used integration by parts). Note that the terms with Π_0 in (3.20) and (3.23) cancel each other. With the help of (3.12) one can transform (3.24) to read

$$\tilde{F}_t \equiv \frac{F_t}{\gamma_0 R_0} \approx -2(\sin\psi_c \cos\theta_c - \sin\theta_c) \int_0^{\pi} \mathrm{d}\sigma \frac{\mathrm{d}\tilde{\zeta}_c}{\mathrm{d}\sigma} \frac{(\lambda^2-1)^{1/2} \sin\sigma \cot\theta_a}{\lambda\cosh\tau_c - \cos\sigma}$$
$$+ \frac{\cos\theta_c}{(\lambda^2-1)^{1/2}} \int_0^{\pi} \mathrm{d}\sigma \left(\frac{\mathrm{d}\tilde{\zeta}_c}{\mathrm{d}\sigma}\right)^2 (\lambda\cosh\tau_c\cos\sigma - 1), \tag{3.25}$$

where $\zeta_c = \tilde{\zeta}(\sigma, \tau_c)$, cf. (2.19). Finally, we recall that the lateral capillary force $\tilde{F}_t$ is to be calculated from (3.14) or (3.25) depending on whether $\tilde{\zeta}(\tau, \sigma)$ is determined by using the boundary condition (2.26) or (2.25), respectively.

4. Numerical results for the lateral capillary forces

4.1. *Numerical results for cork-shaped particles*

Following the procedure described in §2.5 we calculated the meniscus shape, $\zeta(\tau, \sigma)$ and then by using equation (3.14) or (3.25) we determined the capillary force acting on the particles.

Figures 8(*a*) and 8(*b*) present the dimensionless capillary force and the corresponding interaction energy

$$\Delta\tilde{W}(\tilde{L}) \equiv \frac{\Delta W(\tilde{L})}{\gamma_0 R_0^2} = \pi \int_{\tilde{L}}^{1} \tilde{F}_t(\tilde{L})\,\mathrm{d}\tilde{L} \tag{4.1}$$

(which was calculated from the curve $\tilde{F}_t(\tilde{L})$ by means of numerical integration) against the interparticle distance, $\tilde{L}$, for three different particle sizes characterized by θ_c. One sees that the capillary force is negative and corresponds to attraction between the particles. Taking typical values of the parameters ($R_0 = 1$ μm and $\gamma_0 = 30$ mN m^{-1}) one finds that the capillary interaction energy is of the order of (10–100) kT. Here kT is the thermal energy, with k being the Boltzmann constant and $T = 298$ K is room temperature. Such large values of the interaction energy are usual for immersion-type capillary interaction (see Kralchevsky *et al.* 1992, 1993). Physically $\Delta W/kT \gg 1$ means that capillary attraction prevails over the thermal motion and can bring about the particle aggregation and ordering.

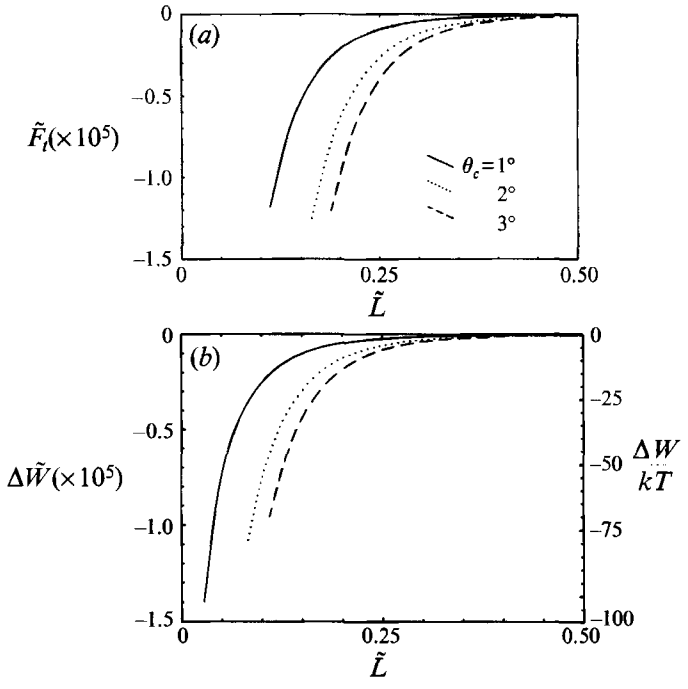

FIGURE 8. (*a*) The capillary force and (*b*) the capillary interaction energy of two cork-shaped particles of fixed contact angle as functions of the interparticle separation, $\tilde{L}$. The different curves correspond to different angle θ_c (i.e. different particle radii). The other parameters are fixed: $qR_0 = 5$ and $\psi_c = 5°$. The right-hand-side scale of $\Delta W/kT$ shows the values of the capillary interaction energy for the special case of $R_0 = 1$ μm, $T = 298$ K and $\gamma_0 = 30$ mN m^{-1}.

Similarly to the values of ΔW, which allow one to judge whether aggregation will happen, the values of F_t in figure 8(*a*) enable one to find whether the particle will move under the action of the capillary force if the friction force is known. For this reason here and hereafter we plot the numerical values of both force and energy *vs.* the interparticle separation.

The counterparts of the curves in figures 8(*a*) and 8(*b*) are presented for particles of fixed contact line in figures 9(*a*) and 9(*b*). The values of h_c/R_0 are chosen to be equal to the respective limiting values h_∞/R_0 (at $\tilde{L} = 1$) in figures 8(*a*) and 8(*b*). In other words, the menisci in the state of zero energy (diametrically opposed particles) are the same for the systems corresponding to figures 8 and 9. This provides a basis for quantitative comparison of the curves for $\tilde{F}_t$ and $\Delta\tilde{W}$ *vs.* $\tilde{L}$ calculated by using the two alternative boundary conditions. One can see in figure 9(*a*) that the capillary force changes its sign at comparatively larger interparticle distances: attractive at short distances becomes repulsive at large separations. The capillary interaction energy (figure 9*b*) exhibits a maximum at some interparticle distance which corresponds to unstable equilibrium. The right-hand-side scale of figure 9(*b*) shows the values of the capillary interaction energy for a typical set of parameters: $R_0 = 1$ μm, $T = 298$ K and $\gamma_0 = 30$ mN m^{-1}.

The fact that the interaction energy can change sign in the case of fixed contact line, but the energy is always negative in the case of fixed contact angle, calls for a special discussion. First we note that the capillary force stems from the inclination of the contact line (see figure 7) in the case of fixed contact angle; mathematically this is expressed through the presence of the derivative $d\zeta/d\sigma$ in (3.25).

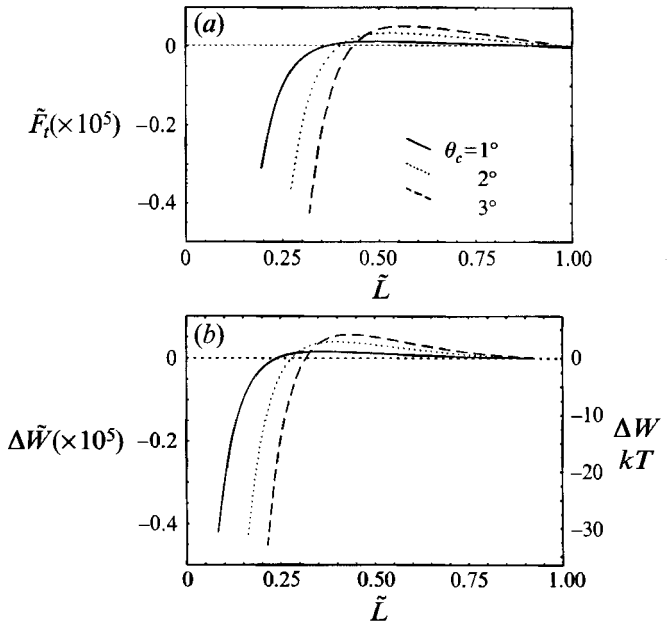

FIGURE 9. (*a*) The capillary force and (*b*) the respective interaction energy of two cork-shaped particles of fixed contact line partially immersed in a spherical liquid layer as functions of the interparticle separation, $\tilde{L}$. The different curves correspond to different values of θ_c; h_c/R_0 is equal to the respective values of h_∞/R_0 (0.00389, 0.00585 and 0.00719) in figure 5(*b*). The capillary length is fixed: $qR_0 = 5$. The right-hand side scale of $\Delta W/kT$ is as in figure 8.

In contrast, one sees that only the derivative $\partial\zeta/\partial\tau$ is present in equation (3.14) expressing the force in the alternative case of fixed contact line. A closer inspection of (3.10) or (3.14) shows that the force is attractive when the meniscus slope, $(\partial\zeta/\partial\tau)/\chi$, at the point $(\tau_c, 0)$ is greater than the meniscus slope at the point (τ_c, π); in the opposite case the force is repulsive. This is confirmed by the direct numerical calculation of $(\partial\zeta/\partial\tau)/\chi$. Our final conclusion is that the non-monotonic behaviour of the capillary force is a non-trivial effect stemming from the spherical geometry of the film coupled with the boundary condition of fixed contact line; such an effect is difficult to anticipate by physical insight. Note that in the case of planar geometry the capillary force between two identical particles is always monotonic attraction.

The influence of the capillary length, q^{-1}, is examined in figure 10 where the dependencies $\tilde{F}_t(\tilde{L})$ and $\Delta\tilde{W}(\tilde{L})$ are plotted for three different values of the parameter qR_0. The larger qR_0 (the smaller the capillary length), the stronger the decay of the capillary force with the distance $\tilde{L}$. Hence q^{-1} can be considered as a decay length of the lateral capillary interaction.

4.2. *Numerical results for spherical particles*

When the boundary condition for fixed contact line, (3.4), is imposed, $\tilde{F}_t(\tilde{L})$ is calculated for spherical particles in the same way as for cork-shaped particles. Indeed, in both cases the contact line is an immobile planar circumference perpendicular to the particle–substrate axis. Hence, the results for spherical particles with fixed contact line are identical with those for cork-shaped particles with the same contact line. In particular, the force and energy are non-monotonic as in figure 9 above.

On the other hand, if the boundary condition for fixed contact angle is imposed, the

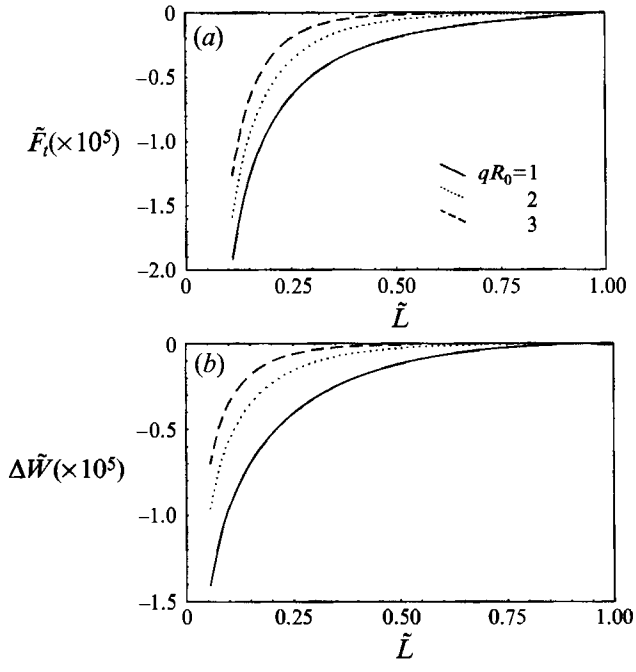

FIGURE 10. (*a*) The lateral capillary force and (*b*) the capillary interaction energy of two cork-shaped particles of fixed contact angle as functions of the interparticle separation, $\tilde{L}$. The different curves correspond to different values of qR_0. The other parameters are $\theta_c = 2°$ and $\psi_c = 3°$.

contact line moves along the particle surface when the interparticle distance is varied. Moreover, one can distinguish two effects when the interparticle separation L decreases: (i) h_c defined by (2.30) increases (figure 5) and (ii) the inclination angle η_c defined by (2.32) also increases. As demonstrated in figure 6, for not too small L, $\tan\eta_c \ll 1$, i.e. the contact line is almost parallel to the reference sphere. This fact allows one to utilize an approximate two-step procedure, which has also been used for planar interfaces (Kralchevsky *et al.* 1992, 1993; Paunov *et al.* 1992). This procedure consists in the following.

As a zeroth approximation we assume that the contact line is perpendicular to the axis determined by the angle θ_a (figure 2*b*). In such a case the contact line is a circumference of radius r_c elevated at an average distance h_c above the reference sphere.

At the next step we replace the sphere by a cork-shaped particle for which θ_c and h_c (as well as ψ_c, θ_a, τ_c, etc.) have the same values. Then we solve numerically (2.23) along with the boundary condition (2.25) and determine $\tilde{F}_t$ by means of (3.25). $\tilde{F}_t$ thus calculated, which is accurate for the cork-shaped particle, gives a first approximation for the lateral capillary force exerted on the spherical particle. Note that when the interparticle separation, L, decreases h_c increases, r_c decreases (figure 2*b*), and therefore at different values of L the spherical particle is approximated by cork-shaped particles of different size (different θ_c). This reflects the shrinkage of the contact line on the spherical particle with the increase of h_c.

The above procedure is realized mathematically as follows. From figure 2(*b*) one sees that the radius of the contact line, r_c, is related to the radius of the reference sphere R_0 and the particle radius R_p:

$$r_c = R_0(1+\bar{h}_c\sin\psi_c)\sin\theta_c = R_p\sin(\alpha+\theta_c+\psi_c), \tag{4.2}$$

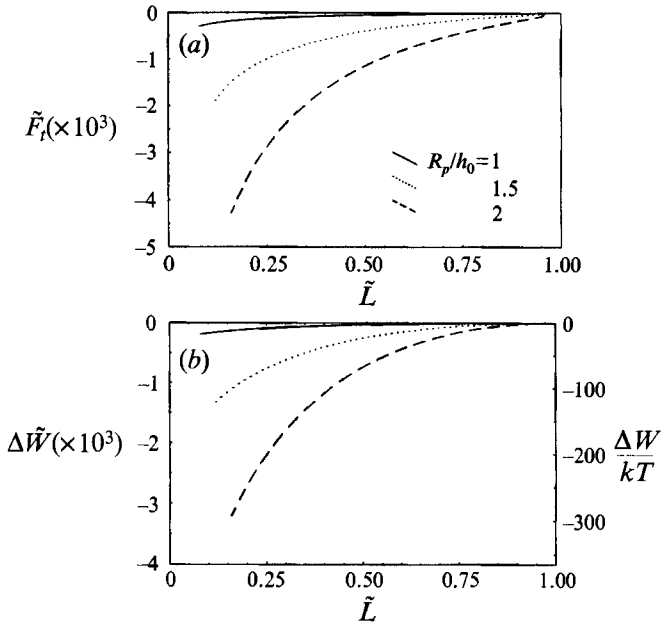

FIGURE 11. (*a*) The lateral capillary force and (*b*) the capillary interaction energy of two spherical particles of fixed contact angle protruding from a spherical liquid layer as functions of the interparticle separation, $\tilde{L}$. The different curves correspond to different values of the ratio R_p/h_0 at fixed $R_p/R_0 = 0.05$. The other parameters are: $qR_0 = 1$ and $\alpha = 60°$. The right-hand-side scale of $\Delta W/kT$ is as in figure 8.

where $\bar{h}_c = \tilde{h}_c/\sin\psi_c$. Note that in contrast with h_c, $\bar{h}_c$ does not depend on ψ_c. For the segment OM one similarly obtains

$$|\mathrm{OM}| = R_0(1+\bar{h}_c\sin\psi_c)\cos\theta_c = R_0 - h_0 + R_p[1+\cos(\alpha+\theta_c+\psi_c)]. \tag{4.3}$$

The angle $\beta \equiv \alpha+\theta_c+\psi_c$ is also shown in figure 2(*b*). From (4.2) and (4.3) one can eliminate angle β to obtain

$$\psi_c(\theta_c) = \arcsin((Y-1)/\bar{h}_c), \tag{4.4}$$

where

$$Y = (1-h_0/R_0+R_p/R_0)\cos\theta_c + [(R_p/R_0)^2-(1-h_0/R_0+R_p/R_0)^2\sin^2\theta_c]^{1/2}. \tag{4.5}$$

The values of R_p/R_0, h_0/R_0, qR_0, α and θ_a are input parameters. Then θ_c and ψ_c are calculated as follows:

(i) we choose an initial guess for θ_c and ψ_c;

(ii) $\tilde{\zeta}$ is calculated by numerical integration of (2.23) along with the boundary condition (2.25), as described in §2;

(iii) then $\bar{h}_c = \tilde{h}_c/\sin\psi_c$ is determined by calculating numerically the integral in (2.30);

(iv) $\psi_c(\theta_c)$ is calculated from (4.4) and (4.5);

(v) θ_c is determined by solving numerically equation (4.2).

The next iteration repeats from point (ii) until convergence is achieved;

(vi) with the parameters values thus determined one calculates $\tilde{F}_t$ from (3.25) for various θ_a.

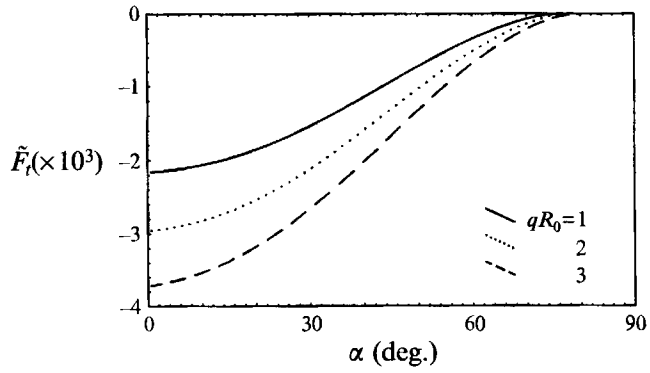

FIGURE 12. The lateral capillary force between two spherical particles as a function of the particle contact angle. The interparticle separation is kept constant ($\sin\theta_a = 2R_p/R_0$). The other parameters are: $R_p/R_0 = h_0/R_0 = 0.05$. The three curves correspond to different values of qR_0.

Following the procedure described above we calculated the force and energy of capillary interaction between two spherical particles immersed into a spherical thin liquid film.

The effect of the particle protrusions from the liquid film on the capillary interaction is shown in figure 11(*a*, *b*) where the dimensionless capillary force and interaction energy are plotted against the interparticle separation, $\tilde{L}$. The three curves are calculated for three different values of the ratio, R_p/h_0, corresponding to different particle protrusions from the film interface. One sees that the larger the protrusions the larger the capillary interaction between the particles. The three-phase contact angle, $\alpha = 60°$ is the same for the three curves. The right-hand-side scale in figure 11(*b*) shows the values of the capillary interaction energy for a typical set of parameters: $R_0 = 1$ μm, $T = 298$ K and $\gamma_0 = 30$ mN m^{-1}. Note that capillary interaction energy between the two particles is of the order of (100–300) kT irrespective of the small values of the particle radius.

Figure 12 illustrates the dependence of the capillary force between two spherical particles on the particle three-phase contact angle, α, at fixed value of the interparticle separation, $\sin\theta_a = 2R_p/R_0$. The thickness of the non-perturbed film, h_0, is chosen to be equal to the particle radius, R_p. The different curves correspond to different values of qR_0. It should be noted that the capillary force between well wettable particles ($\alpha \approx 0°$) is strongest irrespective of the value of qR_0. When α tends to 90° the capillary force approaches zero as could be expected since the deviation of the outer film interface from sphericity becomes negligible.

The effect of the particle radius, R_p, on the capillary interaction is explored in figure 13 where the dimensionless capillary force is plotted *vs.* the ratio R_p/R_0. The three curves correspond to different values of qR_0. One sees that the capillary attraction between the two particles increases markedly with the increase of the particle radius, R_p.

The comparison of figures 12 and 13 with figure 10(*b*) shows an intriguing difference. One sees that when qR_0 increases, the force between spherical particles becomes stronger (figures 12 and 13), whereas the force between cork-shaped particles gets weaker (figure 10*b*). The physical explanation of this fact is the following. In the case of cork-shaped particles the increase of qR_0 brings about a faster decay of the menisci on the two particles, which leads to a smaller overlap of the two menisci and to a weaker lateral capillary force. In the case of spherical particles the latter effect is

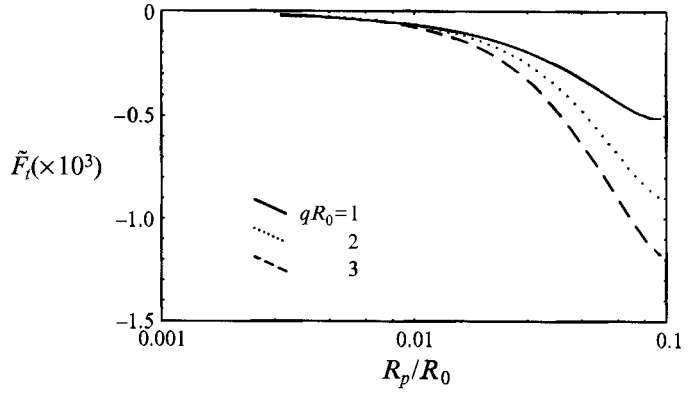

FIGURE 13. The lateral capillary force between two spherical particles of fixed contact angle as a function of the particle radius. The relative interparticle separation is kept constant: $\sin\theta_a = 2R_p/R_0 = \text{const}$. The three different curves correspond to different values of qR_0. The other parameters are $h_0/R_0 = R_p/R_0$.

overcome by another effect in the opposite direction, namely when qR_0 increases, the contact line moves from the top of the sphere downwards (h_c decreases), then both the slope of the spherical surface and angle ψ_c increase, which leads to a stronger attractive force as predicted by equation (3.25). Of course, h_c decreases with the increase of qR_0 for cork-shaped particles also, but angle ψ_c does not change.

5. Concluding remarks

The capillary interaction of two particles partially immersed into a spherical liquid film on a solid spherical substrate is investigated. The study of this system with one deformable interface is the first step toward the investigation of more complicated systems with two deformable surfaces such as a spherical emulsion film or a spherical lipid bilayer (vesicle) containing inclusions. The main points of this study are the following:

The shape of the perturbed liquid film is determined by solving numerically the linearized Laplace equation of capillarity in bipolar coordinates on a sphere, (2.23).

Two types of boundary conditions at the particle surfaces are considered: fixed contact angle and fixed contact line.

Two types of particles are considered: cork-shaped and spherical particles.

Expressions for calculating the lateral capillary force are derived, (3.14) and (3.25), corresponding to the two types of boundary conditions.

The capillary interaction energy corresponds to attraction and is much larger than the thermal energy kT for typical parameters values, and the range of the interaction is determined by the capillary length, q^{-1} – see figures 8, 9, 11 and 13; hence the capillary interaction can bring about particle aggregation and ordering.

For particles with fixed contact angle the capillary interaction energy is a monotonic function of the interparticle distance, whereas for particles with fixed contact line (and not too small qR_0) the interaction energy exhibits a maximum, i.e. the two particles have two stable states (together in aggregate and diametrically opposed) – cf. figures 8 and 9.

Orthogonal bipolar coordinates on a sphere (inducing biconical coordinates in space) are introduced as a helpful instrument for solving this and various other problems – see the Appendix.

This work was supported by the Research and Development Corporation of Japan (JRDC) under the Nagayama Protein Array Project as a part of the program 'Exploratory Research for Advanced Technology' (ERATO). The authors are indebted to Drs K. D. Danov and N. D. Denkov for the useful discussions and to Miss M. Paraskova for typing the manuscript.

Appendix. Bipolar coordinates on a sphere and biconical coordinates in space

Here we propose a system of bipolar curvilinear coordinates on a sphere, which represent two special families of mutually orthogonal circumferences. They induce a system of biconical coordinates in space. Expressions for the spacial metric tensor, Christoffel symbols and the basic differential operators are derived. The rate-of-strain tensor as well as the Navier–Stokes and continuity equations are expressed in terms of these curvilinear coordinates. The latter can find application to any problem in continuum mechanics dealing with particles attached to a spherical interface or liquid film.

A.1. *Bipolar coordinate network on a sphere*

Let us consider a sphere of radius r. The origin of the Cartesian coordinate system is located in the centre of the sphere (figure 14*a*). Let us also consider a plane defined by the equation

$$z = z_0 - (1/\xi)\, x. \tag{A 1}$$

This plane intersects the x-axis at the point $x = z_0\,\xi$, see figure 14(*a*). In addition, the plane cuts a circumference (MN in figure 14*a*) on the sphere. Thus by varying ξ at fixed z_0 one obtains a family of circumferences on the sphere, each of them corresponding to a given ξ for

$$-\xi_{max} \leqslant \xi \leqslant \xi_{max}. \tag{A 2}$$

In fact, this is one of the two families of coordinate lines of the bipolar coordinate system; the poles are the points A_1 and A_2 on figure 14(*a*) corresponding to $\xi = \pm\xi_{max}$.

The equation of a circumference $\xi = \text{const.}$ can be derived by introduction of polar coordinates (θ, ϕ) on the sphere:

$$x = r\sin\theta\cos\phi, \quad y = r\sin\theta\sin\phi, \quad z = r\cos\theta. \tag{A 3)–(A 5}$$

Then from (A 1), (A 3) and (A 5) one derives

$$\cos\theta = \lambda - (1/\xi)\sin\theta\cos\phi, \tag{A 6}$$

where

$$\lambda = z_0/r > 1. \tag{A 7}$$

The coordinates of the two poles are $(\theta = \theta_0, \phi = 0)$ and $(\theta = \theta_0, \phi = \pi)$, where $\cos\theta_0 = r/z_0 = \lambda^{-1}$. Then from (A 6) one derives

$$\xi_{max} = (\lambda^2 - 1)^{-1/2}. \tag{A 8}$$

The second family of coordinate lines, which are also circumferences, represent intersection lines of the plane

$$z = z_1 - (1/\eta)\, y \quad (z_1 = r\cos\theta_0 = r\lambda^{-1} = \text{const.}) \tag{A 9}$$

with the sphere of radius r for fixed z_1 and variable η:

$$-\infty < \eta < +\infty, \tag{A 10}$$

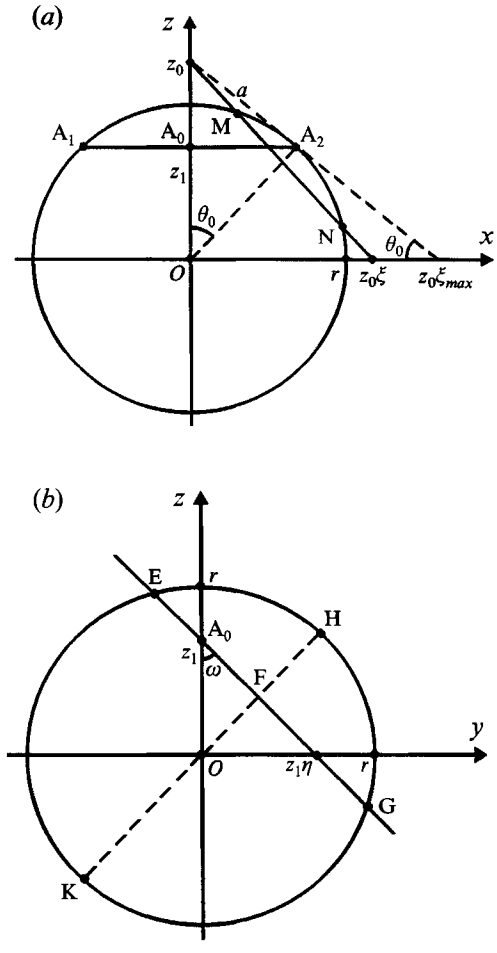

FIGURE 14. Cross-sections of a reference sphere of radius r with the coordinate planes (x, z) (*a*) and (y, z) (*b*). The segments MN and EG represent projections of ξ- and η-circumferences in the plane of the drawing. For $\xi = \pm\xi_{max}$ the ξ-circumferences degenerate into the points A_1 and A_2, which are the poles of the bipolar coordinate network.

see figure 14(*b*). In fact, for each η the plane (A 9) passes through the straight line $A_1 A_2$ determined by the two poles (figure 14*a*). The substitution of (A 4) and (A 5) into (A 9) yields the equation of the η-circumferences in (θ, ϕ)-coordinates:

$$\cos\theta = \lambda^{-1} - (1/\eta)\sin\theta\sin\phi. \tag{A 11}$$

It is interesting to note that these two families of coordinate lines (the ξ- and η-circumferences), which are illustrated in figure 3, are mutually perpendicular: the proof is given in §A 2 below.

One can eliminate the azimuthal angle ϕ between (A 6) and (A 11):

$$\xi^2(\lambda - \cos\theta)^2 + \eta^2(\lambda^{-1} - \cos\theta)^2 = 1 - \cos^2\theta. \tag{A 12}$$

Equation (A 12) is a quadratic equation for $\cos\theta$, whose solution reads

$$\cos\theta = \frac{1}{1+\xi^2+\eta^2}(\lambda\xi^2 + \lambda^{-1}\eta^2 \pm \{[1-(\lambda^2-1)\xi^2][1+(1-\lambda^{-2})\eta^2]\}^{1/2}). \tag{A 13}$$

Let us introduce the variables τ and σ as follows

$$\xi = \frac{1}{(\lambda^2-1)^{1/2}}\tanh\tau, \quad \eta = \frac{1}{(1-\lambda^{-2})^{1/2}}\tan\sigma, \tag{A 14}$$

$$-\infty < \tau < +\infty, \quad -\pi \leqslant \sigma \leqslant \pi, \tag{A 15}$$

cf. also (A 2), (A 8), (A 10) and (A 15). The substitution of (A 14) in (A 13) after some algebra yields

$$\cos\theta = \frac{\cosh\tau - \lambda\cos\sigma}{\lambda\cosh\tau - \cos\sigma} \quad (\lambda > 1). \tag{A 16}$$

For use in applications it is useful to know the radii of the coordinate circumferences. Considering the mutually orthogonal chords EG and KH (figure 14*b*) one can write $|\mathrm{EF}|\cdot|\mathrm{FG}| = |\mathrm{KF}|\cdot|\mathrm{FH}|$. In addition

$$|\mathrm{EF}| = |\mathrm{FG}| = R_\sigma, \quad |\mathrm{KF}| = r + z_1\sin\omega, \quad |\mathrm{FH}| = r - z_1\sin\omega,$$

where R_σ is the radius of a σ-circumference and the other notation is shown in figure 14(*b*). Thus one obtains

$$R_\sigma^2 = r^2(1-\lambda^{-2}\sin^2\omega). \tag{A 17}$$

As $\tan\omega = \eta$ (figure 14*b*), from (A 14) and (A 17) one obtains

$$R_\sigma = \frac{a}{(\lambda^2-\cos^2\sigma)^{1/2}} \quad (a \equiv r(\lambda^2-1)^{1/2}). \tag{A 18}$$

Similarly, for the radius of a τ-circumference one can derive

$$R_\tau = \frac{a}{(\lambda^2\cosh^2\tau - 1)^{1/2}}. \tag{A 19}$$

In the limit of a planar surface ($\lambda \to 1$ for fixed a) both R_σ and R_τ reduce to the respective radii for the planar bipolar coordinate network (see e.g. Korn & Korn 1968).

A.2. *Metric tensor, Christoffel symbols and differential operators*

Substitution of (A 5) into (A 1) and (A 9) yields

$$x = \xi r(\lambda - \cos\theta), \quad y = \eta r(\lambda^{-1} - \cos\theta). \tag{A 20}$$

Then by substituting $\cos\theta$ from (A 16) into (A 5) and (A 20) one obtains

$$x = \frac{r(\lambda^2-1)^{1/2}\sinh\tau}{\lambda\cosh\tau - \cos\sigma}, \quad y = \frac{r(\lambda^2-1)^{1/2}\sin\sigma}{\lambda\cosh\tau - \cos\sigma}, \quad z = \frac{r(\cosh\tau - \lambda\cos\sigma)}{\lambda\cosh\tau - \cos\sigma} \tag{A 21}$$

$$0 \leqslant r < \infty, \quad -\infty < \tau < \infty, \quad -\pi \leqslant \sigma \leqslant \pi.$$

In fact (A 21) gives the connection between the Cartesian coordinates (x, y, z) and the biconical coordinates (r, σ, τ) in space. The latter are induced by the bipolar coordinates on a sphere in the same way as the bicylindrical coordinates in space are induced by the bipolar coordinates in a plane. In our case the coordinate surfaces $\sigma = \text{const.}$ and $\tau = \text{const.}$ represent two families of mutually orthogonal cones.

By differentiation of (A 21) one can derive the components of the metric tensor (McConnell 1957):

$$g_{mn} = \sum_{i=1}^{3} \frac{\partial x_i}{\partial u^m}\frac{\partial x_i}{\partial u^n}, \tag{A 22}$$

$x_1 \equiv x, x_2 \equiv y, x_3 \equiv z; u^1 \equiv r, u^2 \equiv \tau, u^3 \equiv \sigma$. Thus one obtains

$$g_{rr} = 1, \quad g_{\sigma\sigma} = g_{\tau\tau} = \frac{r^2(\lambda^2-1)}{(\lambda\cosh\tau-\cos\sigma)^2}; \quad g_{mn} = 0 \quad \text{for} \quad m \neq n. \tag{A 23}$$

In this way we prove that the biconical coordinates are orthogonal. The relationship between the spatial polar and the biconical coordinates is

$$r = r, \quad \tau = \operatorname{arctanh}\left[\frac{(\lambda^2-1)^{1/2}\sin\theta\cos\phi}{\lambda-\cos\theta}\right], \tag{A 24}$$

$$\sigma = \arctan\left[\frac{(\lambda^2-1)^{1/2}\sin\theta\sin\phi}{1-\lambda\cos\theta}\right]+k\pi, \quad k = \begin{cases} 1 & \text{for} \quad \lambda\cos\theta > 1, \cos\phi > 0 \\ -1 & \text{for} \quad \lambda\cos\theta > 1, \cos\phi < 0 \\ 0 & \text{for} \quad \lambda\cos\theta < 1 \end{cases}$$

By differentiating (A 23) one can derive expressions for the Christoffel symbols by using standard equations (McConnell 1957). The non-zero Christoffel symbols are

$$\begin{Bmatrix} \sigma \\ r\sigma \end{Bmatrix} = \begin{Bmatrix} \tau \\ r\tau \end{Bmatrix} = \frac{1}{r}, \quad \begin{Bmatrix} r \\ \sigma\sigma \end{Bmatrix} = \begin{Bmatrix} r \\ \tau\tau \end{Bmatrix} = \frac{-r(\lambda^2-1)}{(\lambda\cosh\tau-\cos\sigma)^2}, \tag{A 25}$$

$$\begin{Bmatrix} \tau \\ \tau\sigma \end{Bmatrix} = \begin{Bmatrix} \sigma \\ \sigma\sigma \end{Bmatrix} = -\begin{Bmatrix} \sigma \\ \tau\tau \end{Bmatrix} = \frac{-\sin\sigma}{\lambda\cosh\tau-\cos\sigma}, \tag{A 26}$$

$$\begin{Bmatrix} \sigma \\ \sigma\tau \end{Bmatrix} = \begin{Bmatrix} \tau \\ \tau\tau \end{Bmatrix} = -\begin{Bmatrix} \tau \\ \sigma\sigma \end{Bmatrix} = \frac{-\lambda\sinh\tau}{\lambda\cosh\tau-\cos\sigma}. \tag{A 27}$$

All other Christoffell symbols are equal to zero. The gradient of a scalar function $p(r, \tau, \sigma)$ reads

$$\nabla p = \boldsymbol{e}_r\frac{\partial p}{\partial r}+\frac{1}{\chi}\left[\boldsymbol{e}_\tau\frac{\partial p}{\partial\tau}+\boldsymbol{e}_\sigma\frac{\partial p}{\partial\sigma}\right], \tag{A 28}$$

where

$$\chi = \frac{a}{\lambda\cosh\tau-\cos\sigma}, \quad a = r(\lambda^2-1)^{1/2}, \tag{A 29}$$

and $\boldsymbol{e}_r$, $\boldsymbol{e}_\tau$ and $\boldsymbol{e}_\sigma$ are the unit vectors of the local basis. The divergence of a vector $\boldsymbol{v} = \hat{v}_r\boldsymbol{e}_r+\hat{v}_\tau\boldsymbol{e}_\tau+\hat{v}_\sigma\boldsymbol{e}_\sigma$ is

$$\nabla\cdot\boldsymbol{v} = \frac{1}{r^2}\frac{\partial}{\partial r}(r^2\hat{v}_r)+\frac{1}{\chi^2}\left[\frac{\partial(\chi\hat{v}_\tau)}{\partial\tau}+\frac{\partial(\chi\hat{v}_\sigma)}{\partial\sigma}\right]. \tag{A 30}$$

For $\nabla^2 p$ one obtains

$$\nabla^2 p = \frac{1}{r^2}\frac{\partial}{\partial r}\left(r^2\frac{\partial p}{\partial r}\right)+\frac{1}{\chi^2}\left(\frac{\partial^2 p}{\partial\tau^2}+\frac{\partial^2 p}{\partial\sigma^2}\right). \tag{A 31}$$

A.3. *Basic equations of hydrodynamics*

The rate-of-strain tensor is

$$\boldsymbol{D} = \tfrac{1}{2}[\nabla\boldsymbol{v}+(\nabla\boldsymbol{v})^T], \tag{A 32}$$

where $(\nabla\boldsymbol{v})^T$ denotes conjugation

$$\nabla = \boldsymbol{g}^i\frac{\partial}{\partial u^i} \quad \text{and} \quad \boldsymbol{v} = \boldsymbol{g}^k v_k = \boldsymbol{e}_k\hat{v}_k \tag{A 33}$$

are the gradient operator and the velocity vector ($\boldsymbol{g}^k$ ($k = 1,2,3$) are vectors of the contravariant local basis of the curvilinear coordinate system (u^1, u^2, u^3)); summation over the repeated indices is assumed; v_k and $\hat{v}_k$ are the covariant and physical components of v. (From a formal viewpoint the results in the present subsection hold also if $\boldsymbol{D}$ and v are interpreted in terms of theory of elasticity, namely as the strain tensor and displacement vector, respectively). Equation (A 32) can be presented in the form

$$\boldsymbol{D} = \tfrac{1}{2}\boldsymbol{g}^i\boldsymbol{g}^j\left[\frac{\partial v_j}{\partial u^i}+\frac{\partial v_i}{\partial u^j}-2\begin{Bmatrix}k\\ij\end{Bmatrix}v_k\right]. \tag{A 34}$$

In the case of orthogonal coordinates one can write (Korn & Korn 1968)

$$\boldsymbol{g}^k = \frac{\boldsymbol{e}_k}{(g_{kk})^{1/2}}, \quad v_k = (g_{kk})^{1/2}\hat{v}_k. \tag{A 35}$$

By using (A 23), (A 25)–(A 27), (A 34) and (A 35) one obtains

$$\boldsymbol{D} = \boldsymbol{e}_i\boldsymbol{e}_k\hat{D}_{ik}, \tag{A 36}$$

where

$$\hat{D}_{rr} = \frac{\partial \hat{v}_r}{\partial r}; \quad 2\hat{D}_{\sigma\tau} = \frac{\partial}{\partial\tau}\left(\frac{\hat{v}_\sigma}{\chi}\right)+\frac{\partial}{\partial\sigma}\left(\frac{\hat{v}_\tau}{\chi}\right), \tag{A 37}$$

$$\hat{D}_{\sigma\sigma} = \frac{1}{\chi}\frac{\partial\hat{v}_\sigma}{\partial\sigma}-\frac{\hat{v}_\tau}{a}\lambda\sinh\tau+\frac{\hat{v}_r}{r}; \quad 2\hat{D}_{r\sigma} = \frac{1}{\chi}\frac{\partial\hat{v}_r}{\partial\sigma}+\frac{\partial\hat{v}_\sigma}{\partial r}-\frac{\hat{v}_\sigma}{r}, \tag{A 38}$$

$$\hat{D}_{\tau\tau} = \frac{1}{\chi}\frac{\partial\hat{v}_\tau}{\partial\tau}-\frac{\hat{v}_\sigma}{a}\sin\sigma+\frac{\hat{v}_r}{r}; \quad 2\hat{D}_{r\tau} = \frac{1}{\chi}\frac{\partial\hat{v}_r}{\partial\tau}+\frac{\partial\hat{v}_\tau}{\partial r}-\frac{\hat{v}_\tau}{r}. \tag{A 39}$$

The continuity equation and the Navier–Stokes equation for an incompressible fluid are (Landau & Lifshitz 1984)

$$\nabla\cdot\boldsymbol{v} = 0, \tag{A 40}$$

$$\rho\left(\frac{\partial\boldsymbol{v}}{\partial t}+\boldsymbol{v}\cdot\nabla\boldsymbol{v}\right) = -\nabla p+\mu\nabla^2\boldsymbol{v}, \tag{A 41}$$

where ρ is mass density, p is pressure and μ is the dynamic viscosity coefficient. The form of the continuity equation (A 40) in spherical bipolar coordinates follows directly from (A 30). Similarly, ∇p in (A 41) can be expressed by means of (A 28). Further one derives

$$\boldsymbol{e}_r\cdot(\boldsymbol{v}\cdot\nabla\boldsymbol{v}) = \hat{v}_r\frac{\partial\hat{v}_r}{\partial r}+\frac{\hat{v}_\tau}{\chi}\frac{\partial\hat{v}_r}{\partial\tau}+\frac{\hat{v}_\sigma}{\chi}\frac{\partial\hat{v}_r}{\partial\sigma}-\frac{1}{r}(\hat{v}_\tau^2+\hat{v}_\sigma^2), \tag{A 42}$$

$$\boldsymbol{e}_\tau\cdot(\boldsymbol{v}\cdot\nabla\boldsymbol{v}) = \hat{v}_r\frac{\partial\hat{v}_\tau}{\partial r}+\frac{\hat{v}_\tau}{\chi}\frac{\partial\hat{v}_\tau}{\partial\tau}+\frac{\hat{v}_\sigma}{\chi}\frac{\partial\hat{v}_\tau}{\partial\sigma}+\frac{1}{r}\hat{v}_r\hat{v}_\tau+\frac{1}{a}(\hat{v}_\sigma^2\lambda\sinh\tau-\hat{v}_\tau\hat{v}_\sigma\sin\sigma), \tag{A 43}$$

$$\boldsymbol{e}_\sigma\cdot(\boldsymbol{v}\cdot\nabla\boldsymbol{v}) = \hat{v}_r\frac{\partial\hat{v}_\sigma}{\partial r}+\frac{\hat{v}_\tau}{\chi}\frac{\partial\hat{v}_\sigma}{\partial\tau}+\frac{\hat{v}_\sigma}{\chi}\frac{\partial\hat{v}_\sigma}{\partial\sigma}+\frac{1}{r}\hat{v}_r\hat{v}_\sigma+\frac{1}{a}(\hat{v}_\tau^2\sin\sigma-\hat{v}_\tau\hat{v}_\sigma\lambda\sinh\tau). \tag{A 44}$$

To derive an expression for $\nabla^2\boldsymbol{v}$ we use the general formula

$$\nabla^2\boldsymbol{v} = \boldsymbol{g}^k\left[\frac{1}{g^{1/2}}\frac{\partial(g^{1/2}v_k^i)}{\partial u^i}-\begin{Bmatrix}j\\ki\end{Bmatrix}v_j^i\right], \tag{A 45}$$

where g is the determinant of the metric tensor (cf. McConnell 1957). Then after some calculations one obtains

$$\boldsymbol{e}_\tau \cdot \nabla^2 \boldsymbol{v} = \nabla^2 \hat{v}_\tau - \frac{2}{r\chi^2}\left[\frac{\partial(\chi \hat{v}_\tau)}{\partial \tau} + \frac{\partial(\chi \hat{v}_\sigma)}{\partial \sigma}\right] - \frac{2\hat{v}_\tau}{r^2}, \tag{A 46}$$

$$\boldsymbol{e}_\tau \cdot \nabla^2 \boldsymbol{v} = \nabla^2 \hat{v}_\tau + \frac{2}{\chi}\left(\frac{1}{r}\frac{\partial \hat{v}_r}{\partial \tau} + \frac{\lambda}{a}\frac{\partial \hat{v}_\sigma}{\partial \sigma}\sinh\tau - \frac{1}{a}\frac{\partial \hat{v}_\sigma}{\partial \tau}\sin\sigma\right) - \frac{\hat{v}_\tau}{a^2}(\lambda^2\cosh^2\tau - \cos^2\sigma), \tag{A 47}$$

$$\boldsymbol{e}_\sigma \cdot \nabla^2 \boldsymbol{v} = \nabla^2 \hat{v}_\sigma + \frac{2}{\chi}\left(\frac{1}{r}\frac{\partial \hat{v}_r}{\partial \sigma} + \frac{1}{a}\frac{\partial \hat{v}_\tau}{\partial \tau}\sin\sigma - \frac{\lambda}{a}\frac{\partial \hat{v}_\tau}{\partial \sigma}\sinh\tau\right) - \frac{\hat{v}_\sigma}{a^2}(\lambda^2\cosh^2\tau - \cos^2\sigma), \tag{A 48}$$

where $\nabla^2 \hat{v}_k (k = r, \tau, \sigma)$ is to be calculated by means of (A 31). It is worth noting that (A 46), (A 47) and (A 48) hold for every vector $\boldsymbol{v}$, not necessarily satisfying (A 40).

REFERENCES

BRAND, L. 1947 *Vector and Tensor Analysis*. Wiley.

BUSSEL, S. J., KOCH, D. L. & HAMMER, D. A. 1992 The resistivity and mobility functions for a model system of two equal-sized proteins in a lipid bilayer. *J. Fluid Mech.* **243**, 679–697.

CAMOIN, C., ROUSSEL, J. F., FAURE, R. & BLANC, R. 1987 Mesure des forces d'attraction entre sphéres partiellment immergées: Influence des interfaces. *Europhys. Lett.* **3**, 449–457.

CHAN, D. Y. C., HENRY, J. D. & WHITE, L. R. 1981 The interaction of colloidal particles collected at fluid interfaces. *J. Colloid Interface Sci.* **79**, 410–418.

CONSTANTINIDES, A. 1987 *Applied Numerical Methods with Personal Computers*. McGraw-Hill.

DENKOV, N. D., VELEV, O. D., KRALCHEVSKY, P. A., IVANOV, I. B., YOSHIMURA, H. & NAGAYAMA, K. 1992 Mechanism of formation of two-dimensional crystals from latex particles on substrata. *Langmuir* **8**, 3183–3190.

DENKOV, N. D., VELEV, O. D., KRALCHEVSKY, P. A., IVANOV, I. B., YOSHIMURA, H. & NAGAYAMA, K. 1993 Dynamics of two-dimensional crystallization. *Nature* **361**, 26.

DERJAGUIN, B. V., CHURAEV, N. V. & MULLER, V. M. 1987 *Surface Forces*. Plenum.

DUKHIN, S. S., RULIOV, N. N. & DIMITROV, D. S. 1986 *Coagulation and Dynamics of Thin Films*. Naukova Dumka, Kiev (in Russian).

HOCKNEY, R. W. & EASTWOOD, J. W. 1981 *Computer Simulation Using Particles*. McGraw-Hill.

ISRAELACHVILI, J. N. 1977 Refinement of the fluid-mosaic model of membrane structures. *Biochim. Biophys. Acta* **469**, 221–225.

ISRAELACHVILI, J. N. 1992 *Intermolecular and Surface Forces*, 2nd edn. Academic.

IVANOV, I. B. & TOSHEV, B. V. 1975 Thermodynamics of thin liquid films: II Film thickness and its relations to the surface tension and the contact angle. *Colloid Polymer Sci.* **253**, 593–602.

KORN, G. A. & KORN, T. M. 1968 *Mathematical Handbook*. McGraw-Hill.

KRALCHEVSKY, P. A. & IVANOV, I. B. 1990 Micromechanical description of curved interfaces, thin films and membranes. Film surface tension, disjoining pressure and interfacial stress balances. *J. Colloid Interface Sci.* **137**, 234–252.

KRALCHEVSKY, P. A., PAUNOV, V. N., IVANOV, I. B. & NAGAYAMA, K. 1992 Capillary meniscus interaction between colloidal particles attached to a liquid-fluid interface. *J. Colloid Interface Sci.* **151**, 79–94.

KRALCHEVSKY, P. A., PAUNOV, V. N., DENKOV, N. D., IVANOV, I. B. & NAGAYAMA, K. 1993 Energetical and force approaches to the capillary interactions between particles attached to a liquid-fluid interface. *J. Colloid Interface Sci.* **155**, 420–437.

KRALCHEVSKY, P. A. & NAGAYAMA, K. 1994 Capillary forces between colloidal particles. *Langmuir* **10**, 23–36.

LANDAU, L. D. & LIFSHITZ, E. M. 1984 *Fluid Mechanics*. Pergamon.

LEVINE, S. & BOWEN, B. D. 1991 Capillary interaction of spherical particles adsorbed on the surface of an oil/water droplet stabilized by the particles. *Colloids Surfaces* **59**, 377–386.

McConnell, A. J. 1957 *Application of Tensor Analysis*. Dover.

Nagayama, K. 1994 Fabrication of protein crystalline films on mercury. *Materials Sci. Engng* **C1**, 87–94.

Nicolson, M. M. 1949 The interaction between floating particles. *Proc. Camb. Phil. Soc.* **45**, 288–295.

Paunov, V. N., Kralchevsky, P. A., Denkov, N. D., Ivanov, I. B. & Nagayama, K. 1992 Capillary meniscus interaction between a microparticle and a wall. *Colloids Surfaces* **67**, 119–138.

Paunov, V. N., Kralchevsky, P. A., Denkov, N. D. & Nagayama, K. 1993 Lateral capillary forces between floating submillimeter particles. *J. Colloid Interface Sci.* **157**, 100–112.

Petrov, A. G. & Bivas, I. 1984 Elastic and flexoelastic aspects of out-of-plane fluctuations in biological and model membranes. *Prog. Surface Sci.* **16**, 389–511.

Tadros, Th. F. & Vincent, B. 1983 In *Encyclopedia of Emulsion Technology* (ed. P. Becher), vol. 1, p. 129. M. Dekker.

Velev, O. D., Denkov, N. D., Kralchevsky, P. A., Paunov, V. N. & Nagayama, K. 1993 Direct measurements of lateral capillary forces. *Langmuir* **9**, 3702–3709.

Weatherburn, C. E. 1939 *Differential Geometry of Three Dimensions*. Cambridge University Press.

Yoshimura, H., Matsumoto, M., Endo, S. & Nagayama, K. 1990 Two-dimensional crystalization of proteins on mercury. *Ultramicroscopy* **32**, 265–271.